HOKKAIDO UNIVERSITY

Title	Seasonal crustal movements in Northeast Japan revisited
Author(s)	Zheng, Shuo; Heki, Kosuke; Zhang, Zizhan et al.
Citation	Remote Sensing of Environment, 311, 114278 https://doi.org/10.1016/j.rse.2024.114278
Issue Date	2024-09-01
Doc URL	https://hdl.handle.net/2115/97466
Rights	©2024. This manuscript version is made available under the CC-BY-NC-ND 4.0 license https://creativecommons.org/licenses/by-nc-nd/4.0/
Rights(URL)	https://creativecommons.org/licenses/by-nc-nd/4.0/
Type	journal article
File Information	Zheng_etal_RSE2024_Husca.pdf



Hokkaido University Collection of Scholarly and Academic Papers : HUSCAP

Remote Sensing of Environment, 311, 114278, 2024. Doi:10.1016/j.rse.2024.114278

Seasonal crustal movements in Northeast Japan revisited

[1,2]Shuo Zheng, [3, 4*]Kosuke Heki, [1*]Zizhan Zhang, and [1]Haoming Yan

[1]*State Key Laboratory of Geodesy and Earth's Dynamics, Hubei Luojia Laboratory, Innovation Academy of Precision Measurement of Science and Technology, Chinese Academy of Sciences, Wuhan, China*
[2]*University of Chinese Academy of Sciences, Beijing, China*
[3]*Shanghai Astronomical Obs., Chinese Academy of Sciences, Shanghai, China*
[4]*Dept. Earth Planet. Sci., Hokkaido Univ., Japan*

* Corresponding author.
E-mail address: heki@sci.hokudai.ac.jp (Kosuke Heki).
zzhang@asch.whigg.ac.cn (Zizhan Zhang)

Abstract

Seasonal movements of global navigation satellite system (GNSS) stations in Northeast (NE) Japan are mainly driven by elastic loading of snow, reaching a few meters deep along the western flank of the backbone range. Here we study them in a comprehensive manner to solve remaining problems. GNSS stations in the inland area show sharp and strong subsidence peaks in winter and remain flat in other seasons, a response consistent with the snow loading. On the other hand, those close to coasts show broad and weak winter subsidence peaks. This needs additional loads in spring to retard the rapid decay of snow loading. We propose that rice fields work as natural reservoirs until early summer and evaluate quantitative consistency of the hypothesis. We also found that some stations show abnormally large winter subsidence that cannot be explained by snow loading alone. Here we examine two factors, i.e., groundwater extraction in winter for melting snow on roads, and snow accretion onto GNSS antenna radomes. We also evaluate seasonal ocean water mass changes in the Japan Sea using GRACE satellite gravimetry data. We found its role in seasonal crustal movements in NE Japan quite small.

Keywords: Snow loading, seasonal crustal movements, Northeast Japan, GNSS, GRACE, The Japan Sea.

1. Introduction

The elastic responses of the lithosphere to changes in surface loads, such as atmosphere, rainwater, snowpack, and glacier have long been attracting attention of geodesists. In 1980s, they were considered as a “noise”, causing scatters in the time series of station positions in studying crustal movements of tectonic origins. An early work by van Dam and Wahr (1987) was done in this context and pointed out that atmospheric loading may change baseline lengths in very-long-baseline-interferometry (VLBI) by up to 20 mm.

Dense networks of continuous global navigation satellite system (GNSS) stations have been measuring the crustal movements in high temporal and spatial resolution since 1990s. This enabled us to study non-tectonic crustal deformation “signals” of surface hydrological loading as a scientific target. The launch of Gravity Recovery and Climate Experiment (GRACE) satellites in 2002 added a new sensor that can detect surface mass redistribution as time-variable gravity. GNSS and GRACE now plays complementary roles to study surface mass redistribution (Heki and Jin, 2023)

Dong et al. (2002) presented a comprehensive study of seasonal loads and their influence on measurements of crustal dynamics using GNSS. Since then, seasonal crustal movements and hydrological mass changes have been studied in North America (Borsa et al., 2014; Argus et al., 2014; Fu et al., 2014), Iceland (Drouin et al., 2016), Europe (van Dam et al., 2007), and in China (Yan et al., 2019). Recent studies also focus intra-seasonal phenomena such as crustal movements due to rainwater loading by tropical cyclones (Milliner et al., 2018; Zhan et al., 2021) and heavy rain episodes by stationary weather fronts (Heki and Arief, 2022). There are also studies of crustal deformation due to seasonal ocean loading (Alothman et al., 2020; Zheng et al., 2023).

In the Japanese Islands, deployment of a dense network of GNSS receivers in 1990s promoted space geodetic studies of hydrological surface loading. Heki (2001) found

that seasonal crustal movements in NE Honshu, Japan, are driven mainly by winter snows. Later, Heki (2004) performed a comprehensive study of various seasonal surface loading, such as atmosphere, soil moisture, impoundment of dams, non-tidal ocean loading, in addition to snow, over the whole Japanese Islands and demonstrated that the snow exerts the largest contribution in NE Japan. This led to investigation of the relevance of seasonal seismicity to snow loads (Heki, 2003; Ueda et al., 2024).

Over the last two decades, further densification of the network and longer time span made it possible for us to address new issues. For example, we can discuss inter-annual changes in amplitudes of seasonal subsidence and snow depths, and discuss their relevance to climate changes. We can also compare waveforms of seasonal changes between crustal subsidence and snow loads.

It is also possible to discuss quantitative consistency of their amplitudes. This further lets us investigate issues such as the link of abnormally large winter subsidences seen at some GNSS stations, to factors other than snow loading, e.g., groundwater extraction for melting snow on roads and snow accretion onto GNSS antenna radome. Systematic studies are needed to clarify the contributions of such factors to winter subsidence signals.

Accumulation of time variable gravity data enables us to study ocean mass changes more precisely. Because of insufficient length of the GRACE data, Heki (2004) could not adequately model seasonal changes in non-tidal ocean loading around Japan. Although the seasonal mass changes in the Pacific Ocean is small, the Japan Sea, a semi-closed ocean, may significantly contribute to seasonal crustal deformation in NE Japan. Here we study seasonal mass change signals in the Japan Sea using GRACE and altimetry data. We then discuss its contribution to seasonal crustal movements in NE Japan.

2. Data and Methods

2.1 GNSS station position data

We obtained the time series of GNSS station positions in local coordinates from the

Nevada Geodetic Laboratory (Blewitt et al., 2018) to study seasonal crustal movements in NE Japan. Here we use vertical coordinate time series of 685 GNSS stations of GNSS Earth Observation Network (GEONET), operated by Geospatial Information Authority of Japan, in 2012–2021 (**Fig.1A**) from snowy areas in NE Japan, where maximum snow depths range from a few tens of centimeters to a few meters (**Fig.1B**). To obtain accurate estimates of seasonal terms, we selected stations with at least 4 years of recorded data with a minimum data availability of 60.0%. Then, we select 480 stations satisfying these criteria. We use the third quartile criterion (He et al., 2020) to eliminate the outliers in the raw GNSS time series.

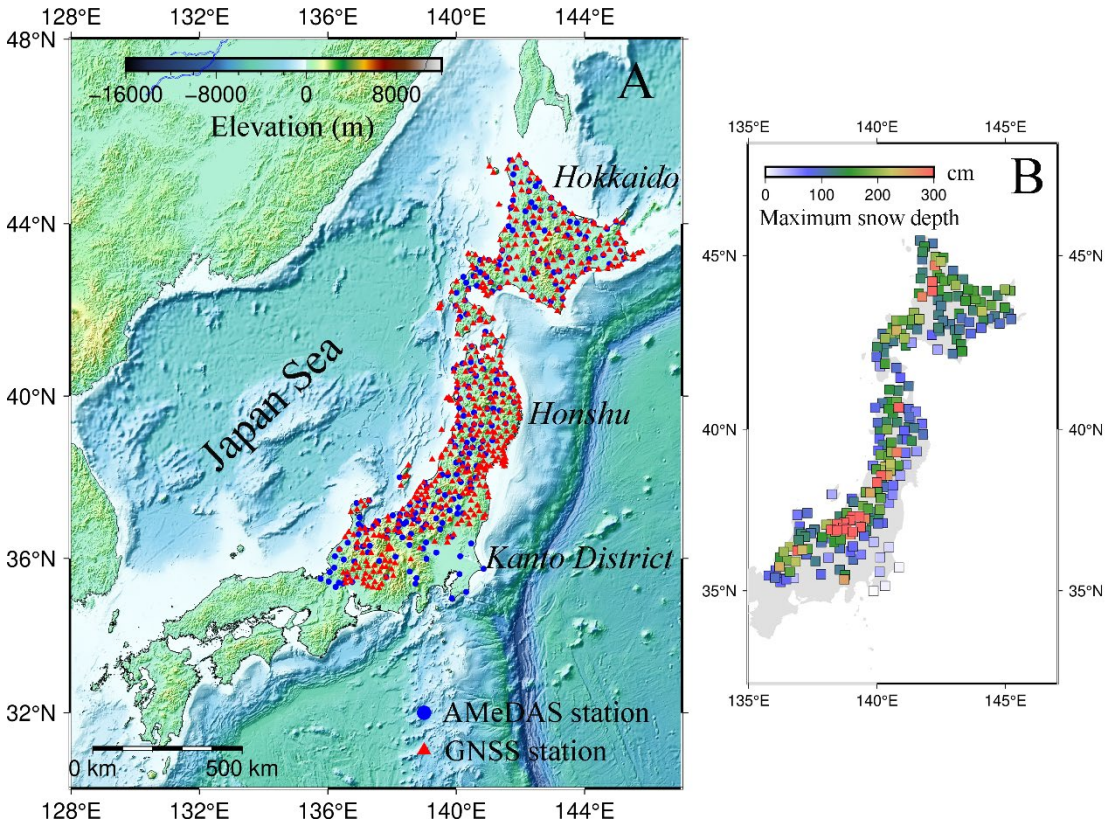


Fig. 1. (**A**) The distribution of continuous GNSS and Automated Meteorological Data Acquisition System (AMeDAS) stations in regions covered with snow in winter in Japan. (**B**) The squares show average values of maximum snow depths over ten winters 2012-2021 at AMeDAS stations.

To estimate the vertical seasonal crustal movements associated with the snow load in Japan, we corrected for the non-tidal atmospheric loading (NTAL) effects (**Fig. S1**)

for GNSS coordinate time series using the products released by the Earth System Modeling group at Deutsches GeoForschungsZentrum (ESMGFZ, http://esmdata.gfz-potsdam.de:8080/repository). However, we have not corrected non-tidal oceanic loading (NTOL) effect because the ocean loading is one of the targets of our study.

The GNSS daily vertical position time series were modeled with a set of estimated parameters composed of linear trends, seasonal terms, instrumental offsets, coseismic jumps and postseismic logarithmic decays (relaxation time assumed as 67 days) by least-squares regression. Then the residual series were used to calculate the common mode error (CME) following the method in Zheng et al. (2023). We first remove seasonal components and linear trends, and then estimated the CME using principal component analysis. After removing the CME, seasonal components, removed beforehand, has been added back (Kierulf et al., 2021).

2.2 Snow depth data in NE Japan

To infer snow mass in NE Japan, we use the daily averages of the snow depth data at stations of the Automated Meteorological Data Acquisition System (AMeDAS), operated by the Japan Meteorological Agency. In this study, we chose 228 stations with continuous data in 2012–2021 (**Fig.1A**). For later use, we also made monthly averaged snow depth data sets.

The snow depth distribution is highly heterogeneous in NE Japan (**Fig.1B**). The largest snow depths are seen in the western flanks of the backbone range. The snow depth decreases rapidly toward the Japan Sea coast. Also, the snow depths are much less to the east of the backbone range and along the Pacific Ocean coast. **Fig. 2** shows the diversity of snow depths along the line of ~37°N. The maximum depths occur from late February to early March. The snow rapidly melts in April and remains absent until December. Hence, snow loading generally has a strong peak in winter and long flat period from spring to autumn.

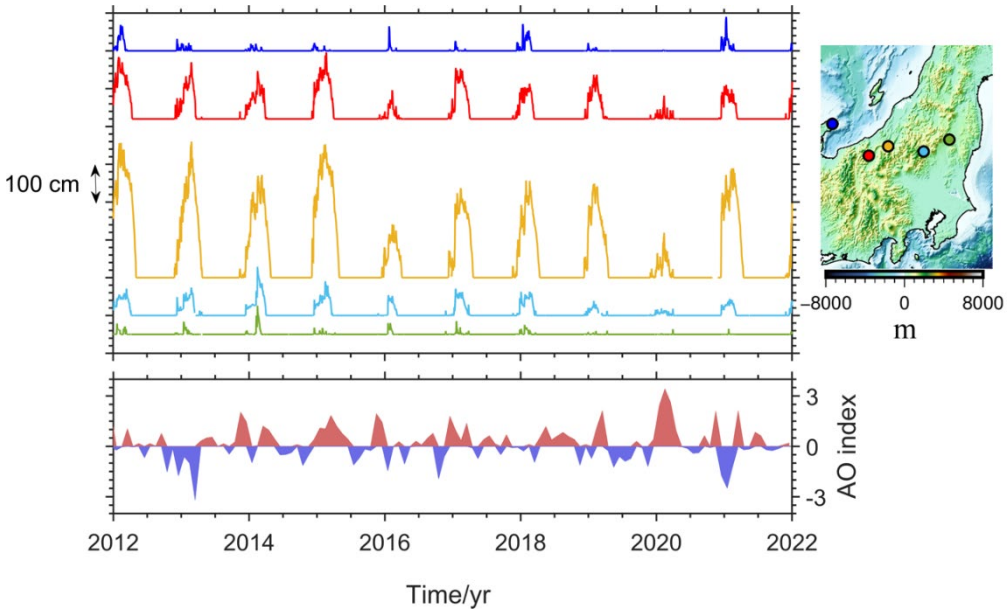


Fig. 2 Daily snow depths during 2012–2021 at five AMeDAS stations distributed along the latitude ~37°N. The colors of the curves correspond to those shown in the map. Their names and prefectures are, from west to east, Suzu (Ishikawa), Shinano-machi (Nagano), Tsunan (Niigata), Dorobu (Tochigi), and Shirakawa (Fukushima). Their interannual variation seems negatively correlated with the AO index (https://www.ncei.noaa.gov/access/monitoring/ao/) shown at the bottom.

There are significant interannual changes in snow depths, e.g., snow during the 2019-2020 winter is much less than the 2020-2021 winter. Matsuo and Heki (2012) showed, at this latitude, amounts of the winter snow are negatively correlated with the Arctic Oscillation (AO) index, representing the see-saw-like fluctuation in the sea level pressure between polar and middle latitude regions of the Northern Hemisphere. **Fig. 2** suggests this is the case to some extent. This index recorded 3.4 in Feb 2020, the highest value since 2002. This made the snow depth in the 2019-2020 winter lowest in the studied period. However, this does not necessarily mean that the subsidence was the smallest. This will be discussed again in Section 5.1.

2.3 Data of the Japan Sea

2.3.1 GRACE time-variable gravity

In order to investigate water mass changes in the Japan Sea, we used the monthly GRACE/GRACE-FO RL06 gravity solutions, provided by the Center for Space

Research (CSR), University of Texas at Austin, in the form of fully normalized spherical harmonic (SH) coefficients (the Stokes' coefficients) complete to degree and order 60. We used the data covering the interval 2012-2021.

The degree 2 order 0 (C_{20}) coefficients in the GRACE solutions were replaced with those from satellite laser ranging (SLR) provided by CSR (Cheng et al., 2011). We also used the degree-1 coefficient from Swenson et al. (2008), estimated based on the ocean and atmospheric models, to correct for geocenter motion. To minimize north-south stripe noises in the monthly SH solutions, the P4M6 decorrelation filter was used (Swenson and Wahr, 2006; Chen et al., 2017), and the Gaussian filter with a 300-km radius was further applied to reduce the high-frequency noise (Wahr et al., 1998).

We also used the monthly GRACE/GRACE-FO RL06 mascon solutions from CSR (Save et al., 2016; Save et al., 2019), represented on 0.25°×0.25° latitude-longitude grid to compare with GRACE SH data products at commensurable spatial resolution.

2.3.2 Sea surface height changes and steric correction using data from ARGO

To compare with the GRACE data, we also use sea surface height data in the Japan Sea. We use the data set from the Copernicus Marine Environment Monitoring Service (CMEMS), called Global Ocean Gridded L4 Sea Surface Heights and Derived Variables Reprocessed 1993 Ongoing. It has a monthly temporal resolution and a spatial resolution of 0.25°×0.25°. The dataset covers the time period from January 1993 to the present. The Sea-level anomalies are computed by removing the mean sea surface height over 1993 to 2012 (Pujol and Francoise, 2016). We also use monthly water-level records from 6 tide gauges along the eastern margin of the Japan Sea archived at the Permanent Service of Mean Sea Level (PSMSL).

Water temperature and salinity changes lead to steric changes in the sea surface height (SSH) of the Japan Sea. Therefore, we use the data from the Array for Real-Time Geostrophic Oceanography (ARGO) float, an ocean surveillance system deployed to measure the temperature and salinity profiles of the upper 2000 m of the ocean (Roemmich and Owens, 2000; Argo, 2000). We used the global gridded ARGO data 2012-2021 at 1° grid spacing and one-month temporal sampling, with a depth range of

0-2000 dbar, to compute average monthly steric sea level changes in the Japan Sea.

3. Seasonal mass changes

3.1 Conversion of snow depth to snow mass

Snow depths need to be converted to snow mass to discuss crustal deformation due to snow loading. Heki (2004) pointed out that the AMeDAS stations tend to be deployed along the well-populated valleys, i.e., they are sparse in mountain regions. Because snow depths depend strongly on elevation, this causes significant underestimation of snow depths. Here we follow Heki (2004) to infer more realistic snow depth distribution.

First, we divide the studied region into prefectures. Japan has ~60 prefectures, and a typical prefecture is composed of a plain/basin and surrounding mountain ranges. We first confirm linear relationship between station altitudes and snow depth within individual prefectures, and estimate two coefficients (slope and bias) for each of them. Then, we convert observed snow depths within prefectures into those at their average altitudes. Although detailed information on small-scale snow distribution is lost, this correction makes the snow depth realistic (Heki, 2004) (**Fig. S2**). For this calculation, we used average values of maximum snow depths of 10 winters 2012-2021 (**Fig.1B**). In Section 5.1, we compare observed subsidences with those calculated using snow depths before and after this correction to justify this procedure.

To discuss the snow loading, we need the density of snow to convert snow depths to mass. Here we assume the time-dependent snow density proposed by Heki (2004) based on in-situ density measurements, i.e., it linearly increases from 250 kg/m^3 at the start of December by 40 kg/m^3/month, attaining 400 kg/m^3 at the end of March.

3.2 Seasonal mass changes in the Japan Sea

3.2.1 GRACE data

Here we infer seasonal water mass changes in the Japan Sea based on satellite gravimetry data. **Fig. 3** compares curves of average seasonal mass changes at points within the Japan Sea from GRACE SH and mascons. There, monthly data are modeled

with linear functions and seasonal (annual and semiannual) terms, and we show seasonal terms there. They are fairly uniform in the middle and western parts of the sea. The SH and mascon solutions show overall consistency in the amplitude and phase. They have peak-to-peak amplitudes of ~5 cm with the minimum and maximum around June and October, respectively.

In contrast, in the eastern part of the Japan Sea, both SH and mascon estimates show two peaks in a year, i.e., the secondary peak emerges in March in addition to October. We suspect that the March peak is not real but indicates the leakage of snow mass signals on land. Similar March peaks exist both in the SH and the mascon solutions, although the latter is somewhat smaller. The mascon data at (137E, 39N) and (139E, 39N) showed anomalously large variations due to unknown reasons.

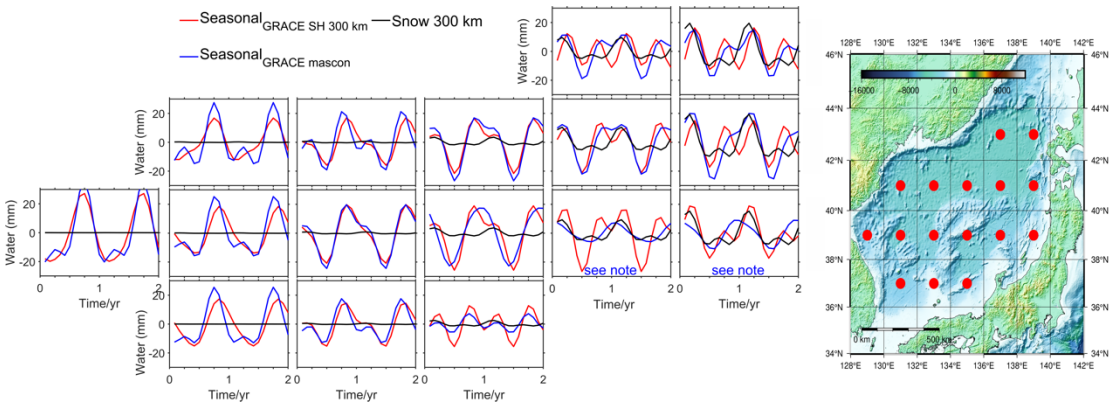


Fig. 3. Comparison of seasonal mass changes between the GRACE SH (red) and mascon (blue) solutions. The black curves indicate the numerically simulated leakage of land snow signal to the Japan Sea. The location of each panel to the left is represented by the red dot in the map. Mascon data at the two grid points in southeastern part (marked as "see note") are anomalously large and are reduced to 10 % in these two panels.

We conducted a numerical experiment to confirm this leakage. We used the snow mass obtained in Section 3.1 and used the Spatial Structure Function (SSF) method (Hammond et al., 2016) to interpolate them to 0.5° × 0.5° grid data. We first represent the snow mass field in the wavelength domain using SH complete to degree and order

60. We then apply the 300-km Gaussian filter (Wahr et al., 1998) (degree-0 and -1 terms are set to zero) and convert them into space domain to calculate values at grid points in the Japan Sea.

The results are shown as black curves in **Fig. 3**. They have significant peaks in March at points close to NE Japan, with amplitudes roughly consistent with those in the SH solutions. Hence, the secondary peak in March comes from the leakage of the snow mass, and the entire Japan Sea has just one maximum in ocean mass in October and minimum in June. We also obtained seasonal mass changes in the Pacific Ocean near NE Japan using the GRACE data and found that their amplitudes are <1/3 of those in the Japan Sea.

3.2.2 Satellite altimetry and in-situ data

To compare with the GRACE data, we show seasonal ocean mass changes inferred by combining the satellite radar altimetry data and ARGO in-situ measurement data. We use altimetry data to see total SSH changes and ARGO float data to remove steric components within them. Considering sparse distribution of the ARGO data, we employ $3^o \times 3^o$ grid.

Tide gauges in the Japan Sea coast of NE Japan show large changes in SSH with amplitudes 10-15 cm (**Fig. S2**). Similar seasonal changes in SSH are also confirmed by satellite altimetry. Steric components from the ARGO float also show large seasonal variations. The SSH and steric components change nearly in phase, i.e., amplitudes are much reduced by taking their difference (**Fig. 4**). Nevertheless, we get ~5.0 cm peak-to-peak seasonal changes.

The altimeter-ARGO results are in good agreement with the GRACE data in seasonal time scales (**Fig. 4**). The altimeter-ARGO only show one peak around October because the data are free from the leakage of the land snow signals. The agreement between GRACE and altimeter-ARGO estimates confirms that mass change in the Japan Sea is ~5.0 cm in peak-to-peak with the peak in late autumn. The peak of ocean loading is not so sharp as that of the snow, and the change is similar to an annual sine curve.

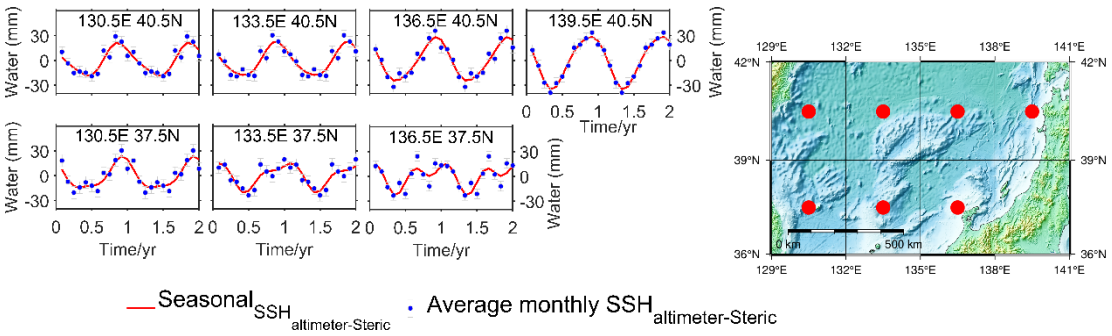


Fig. 4. Seasonal mass changes in the Japan Sea at 3° × 3° grid points, from satellite altimeter observations after correction of steric components from the ARGO data. The original data (blue dots) are modeled with best-fit seasonal (annual and semiannual) curves (red curve). The locations of the grid points are represented by the red circles in the map.

4. Seasonal vertical movements of GNSS stations

4.1 Two types of waveforms

Here we study observed seasonal vertical crustal movements of GNSS stations in the snowy region of the Japanese Islands. We find their behaviors are somewhat different between two groups, i.e., the stations in the inland region and those on the Japan Sea coast. **Fig. 5** compares the time series at three GNSS stations from each group. The two groups have sharp and broad winter subsidence peaks, respectively.

The inland stations show short and strong subsidence peaks in February/March. They resemble to snow depth curves (**Fig. 2**) and can be interpreted straightforward as elastic response of the lithosphere to the snow load. The coastal stations show broad and weak winter subsidence peaks. The maximum subsidence occurs also in February/March, but significant subsidence continues until the end of spring. As a whole, it resembles more to the mass changes of the Japan Sea (**Fig.3**) rather than snow. However, quantitative consistency between the winter subsidence and the ocean mass changes should be confirmed. We will discuss this later in Section 5.3.1.

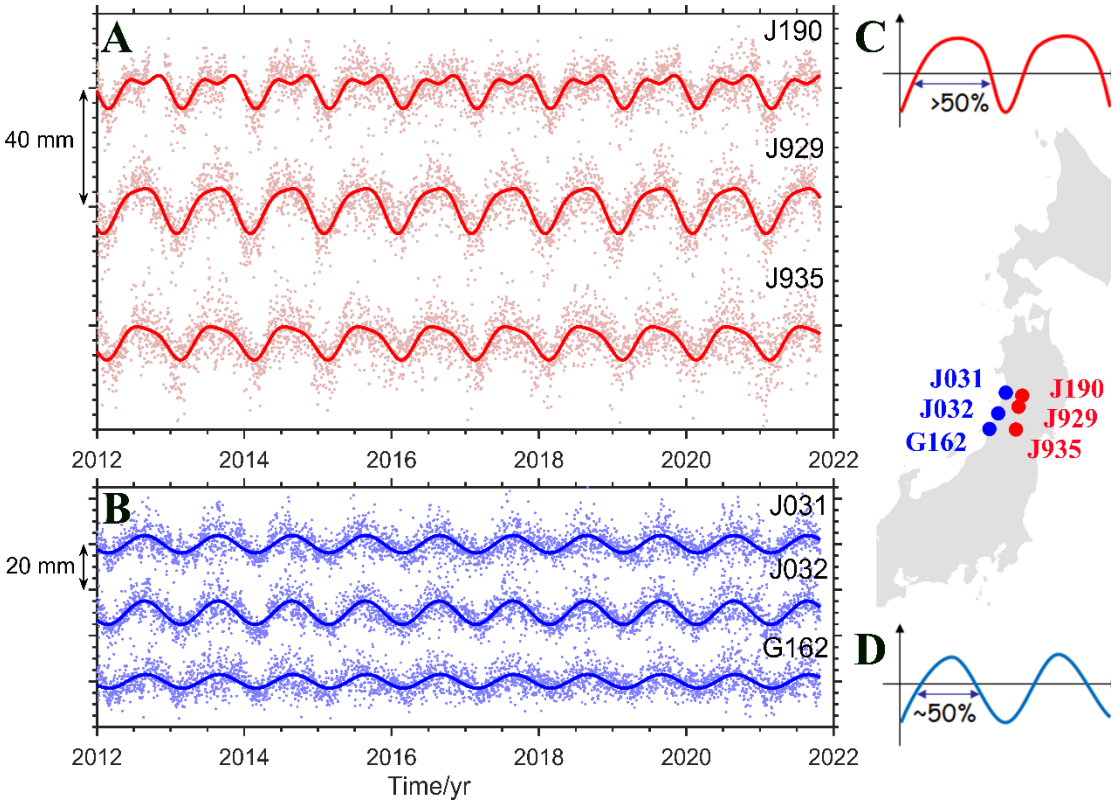


Fig. 5. The up component time series of six GEONET GNSS stations (dots in the inset map) are shown together with average seasonal (annual and semiannual) change curves. The three of the six GNSS stations are in the snowy inland area (red circles in the map) (**A**), and the other three are located along the Japan Sea coast (blue circles in the map) (**B**). The waveform of the former group has the ratio of the positive part of the annual changes >50% (**C**), while that of the latter group is ~50% (**D**).

To quantify the difference in waveforms, we introduce a new index indicating the percentage of the positive part of the average seasonal changes. The index shows the proportion of the days showing positive deviation from the average. If the ratio significantly exceeds 50%, it has the sharp winter subsidence peak (**Fig. 5C**). On the other hand, the ratio would remain ~50% for the coastal stations, and the seasonal changes would look like a sine curve (**Fig. 5D**). We try to quantify the waveforms of GNSS stations using this index.

Fig. 6 shows the distributions of the new index. It will be discussed in the next section (Section 4.2), some of the stations do not subside in winter, and we exclude them in **Fig.6**. We can see that the two types are systematically distributed, i.e., sharp winter peaks are dominant along the mountain range. As shown in **Fig. 1B**, this distribution

overlaps with heavy snow regions. This suggests that the signature reflects sharp subsidence peaks by snow loading in winter months. The rapid termination of the winter subsidence would correspond to the rapid snow melting and runoff in April. On the other hand, stations having the broad winter peaks are distributed along the Japan Sea coast and also widespread in the eastern side of the backbone range.

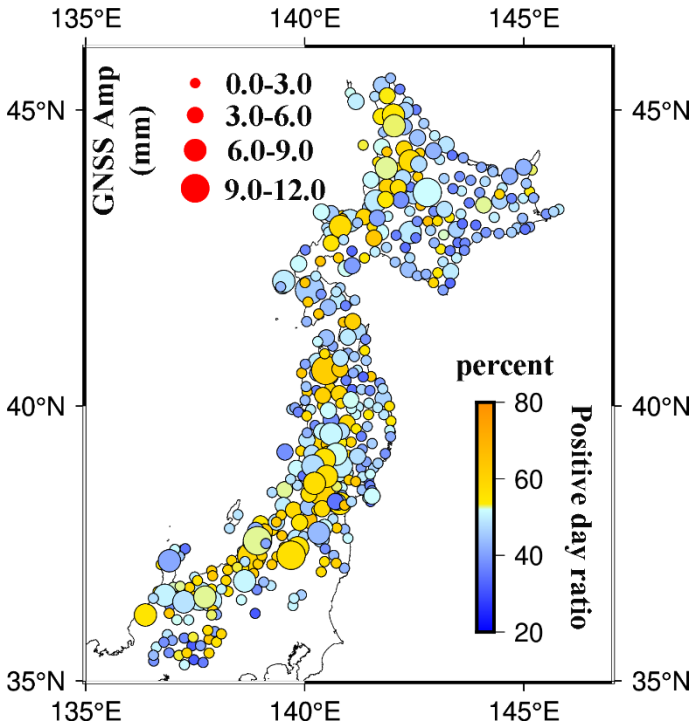


Fig. 6. The colors show the percentage of the positive day in the average seasonal changes for GNSS stations in the snowy area of NE Japan. The sizes of the symbols indicate the peak-to-peak amplitudes of seasonal vertical movements. Yellow stations (with sharp winter subsidence peaks) tend to have larger amplitudes and are located in inland regions with deep snow.

4.2 Phase consistency

We define the amplitudes of vertical crustal movements in peak-to-peak. Before comparing the amplitudes of the winter subsidence of GNSS stations with snow loading, we confirm the phases of the seasonal movement, i.e., if the stations in the studied area (area covered with snow in winter) really subside in winter. Here we assume that the maximum snow loading should occur on March 1. We then calculate the difference of the maximum subsidence day in average seasonal vertical movement curves from this nominal day. The differences, converted to degrees, are plotted in **Fig. 7**. As expected,

stations in the snowy area show small deviations, suggesting that the subsidence does occur in winter due to snow loading.

We notice that some of the GNSS stations located in the Pacific Ocean side subside in other seasons. Their amplitudes are relatively small, typically a few mm. Thus, it may merely reflect large errors in determining maximum subsidence times out of noisy vertical position time series. For stations close to the Kanto District, summer subsidence may actually occur by extracting groundwater for impoundment in rice fields (Munekane et al., 2004). Whatever the reason, we excluded stations with phase differences >100 degrees from discussions on the consistency between the observed and calculated (assuming snow loading) subsidences in Section 5.1.

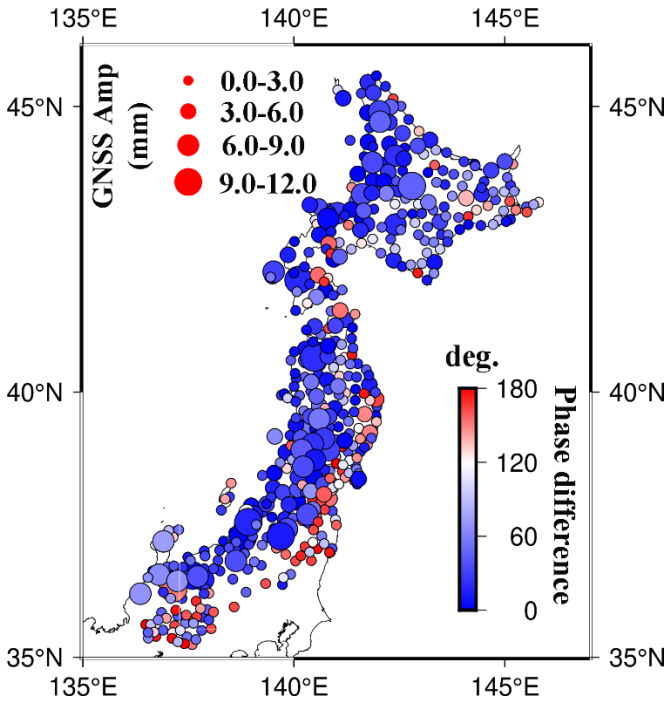


Fig. 7. The color of the circles shows the differences of the observed phase of maximum subsidence of GNSS stations from March 1. The sizes of the circles reflect annual vertical crustal displacement amplitudes of GNSS stations. Stations with small amplitude (stations shown with the smallest circles) often show significantly different subsidence peaks, and these stations are excluded from subsequent discussions.

5. Discussions

5.1 Amplitudes of winter subsidence and snow loading

As described in Section 3.1, we converted snow depth data to realistic snow loading by two steps following Heki (2004), first correcting for biased altitude distribution of snow depth meters, and secondly multiplying snow depths with time-dependent snow density. Then we used the SSF method to interpolate the monthly snow mass data to 0.5° × 0.5° grid data in latitude and longitude and calculated subsidence of GNSS stations using the Green's function (Farrell, 1972) (see Section 3.2.1 for detail).

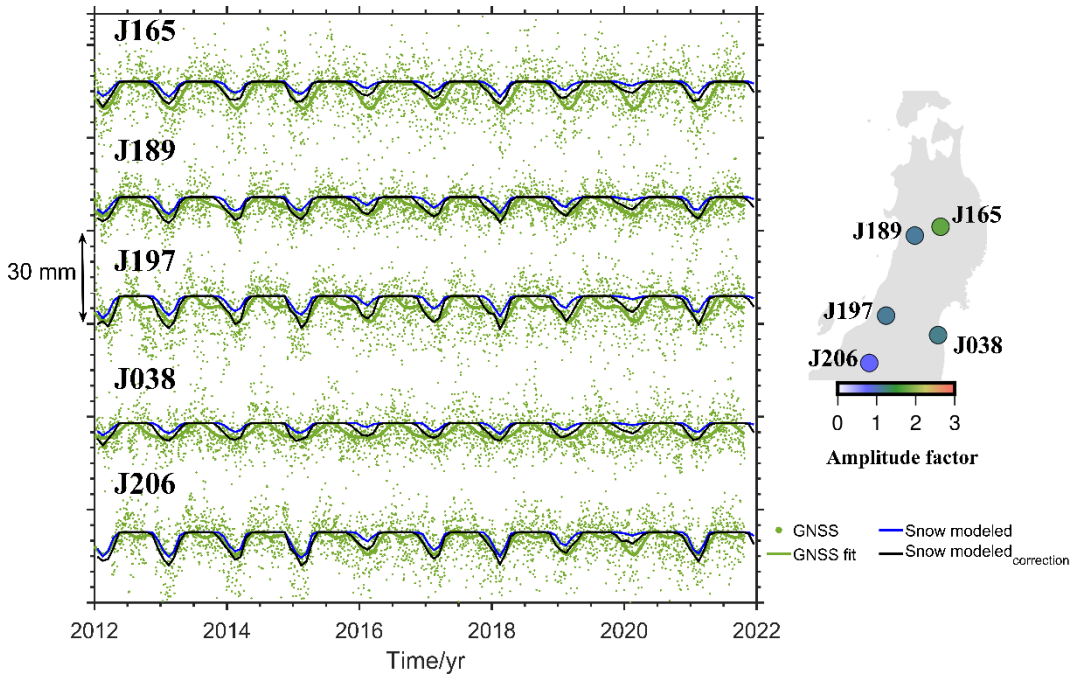


Fig. 8. Detrended time series of up components (green dots) of five GNSS stations in the map, compared with the modeled curves based on the observed snow depths, modeled snow density, and the Green's function (black curves). Thick green curves indicate average seasonal (annual and semiannual) change curves estimated using the observations. We also show modeled curves based on the snow depths before the altitude correction (blue curves). The colors of the GNSS stations in the map indicate the ratio of the observed winter subsidence to those calculated (with corrected snow depths).

Fig. 8 shows time series of the observed vertical positions of GNSS stations in NE Japan and compares them with two different calculated subsidences, those with and without the altitude correction described in Section 3.1. We can see that the latter significantly underestimates the observed subsidence, reflecting the negative biases of

snow depths by the AMeDAS stations. On the other hand, the former is mostly consistent with the observations.

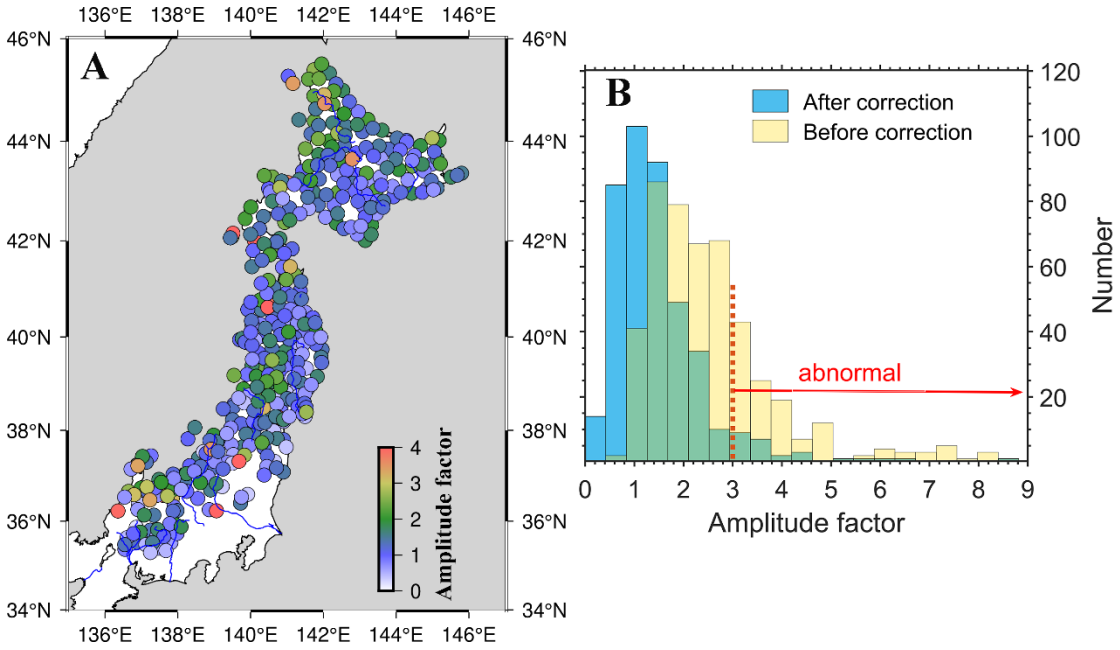


Fig. 9. (A) The distribution of the amplitude factors, the ratios of the observed subsidence to the modeled values. Stations with small (<3 mm) observed amplitudes in Fig. 8 have been already removed. **(B)** A histogram in blue showing the distribution of the amplitude factor shown in **(A)**. These factors distribute around unity. We show the distribution of stations showing the factor exceeding 3 (marked as "abnormal") in **Fig. S4**. The yellow histogram represents the amplitude factor calculated using raw snow depth data before the altitude correction.

Color in the inset map of **Fig.8** shows the ratio (amplitude factor) of the observed winter subsidences relative to those of average seasonal changes of the modeled subsidence (with the altitude correction). They are not much different from unity for these 5 examples. **Fig. 9A** shows the distribution of the amplitude factors for all the GNSS stations. If we calculate the factors using the raw snow depths, only ~40% of the GNSS stations show the factors between 0.5 and 1.8 (yellow histogram, **Fig.9B**). By using altitude-corrected snow depth data, this improves to ~80% (blue histogram, **Fig.9B**), suggesting that the altitude correction was reasonable. Stations showing amplitude factors exceeding 3 are shown in **Fig. S4**. They suffer from multiple problems, which will be discussed in Section 5.2.

In Section 2.2, we showed snow depth curves have large inter-annual variations. A clear example is the comparison of the subsidences in the 2019-2020 winter with those in the 2020-2021 winter. **Fig.2** shows that the snow depth of the former is less than a half of the latter. This is reflected in the difference of the modeled crustal subsidence in **Fig.8** (blue and black curves). As demonstrated in Heki and Jin (2023), we expect to see this contrast also in the observed crustal subsidence (green dots in **Fig.8**). However, the contrast is not so clear in **Fig.8**, nor in **Fig.5**. This suggests that one half snow depth may not always mean one half loading. A thinner snowpack of that winter was caused by a higher temperature and less snow (JMA, 2021). Then, occasional warm rains may have reduced the snowpack thickness, making snow wet and increasing its density. As a result, the loading may not have been so weak as inferred from the small snow depth.

5.2 Origins of abnormally large subsidences

5.2.1 Groundwater extraction

Fig.9A includes 25 stations with a factor exceeding 3 (marked as "abnormal" in **Fig.9B**). Abnormal subsidences of these stations (for geographical distribution, see **Fig. S4)** would come from multiple reasons. If the abnormal subsidence is episodic, i.e., lasting only for short-terms (a few days to a week) and recovering suddenly, one would doubt snow accretion onto the GNSS antenna radomes (Heki and Jin, 2023). If the abnormal subsidence lasts over the whole winter, one should doubt the groundwater extraction for snow melting (Sato et al., 2003; Matsumoto et al. 2018; Morishita et al., 2020).

Fig. 10 shows time series at four of those stations, J540, J033, J939, and J240. They are located within urban areas as shown in the **Fig. 10** inset map. They are either within a plain near the Japan Sea coast or basins in the western flank of the backbone range. Their winter subsidences far exceed expected values. Indeed, those at J240 exceed 10 cm. Their time series are quite unique. Although they have sharp onsets of subsidence at the beginning of winter, the subsidences recover gradually during summer and autumn.

We consider that the excessive winter subsidences at these stations are due to artificial ground water extraction. In snowy regions with relatively high winter temperatures, local authorities often pump groundwater from aquifer. They let it flow freely on busy roads in city centers so that snows on roads rapidly melt. This causes shrinking of the aquifers and amplifies snow load signatures of winter subsidence. The recovery of the aquifers may last until late autumn as suggested by the time series.

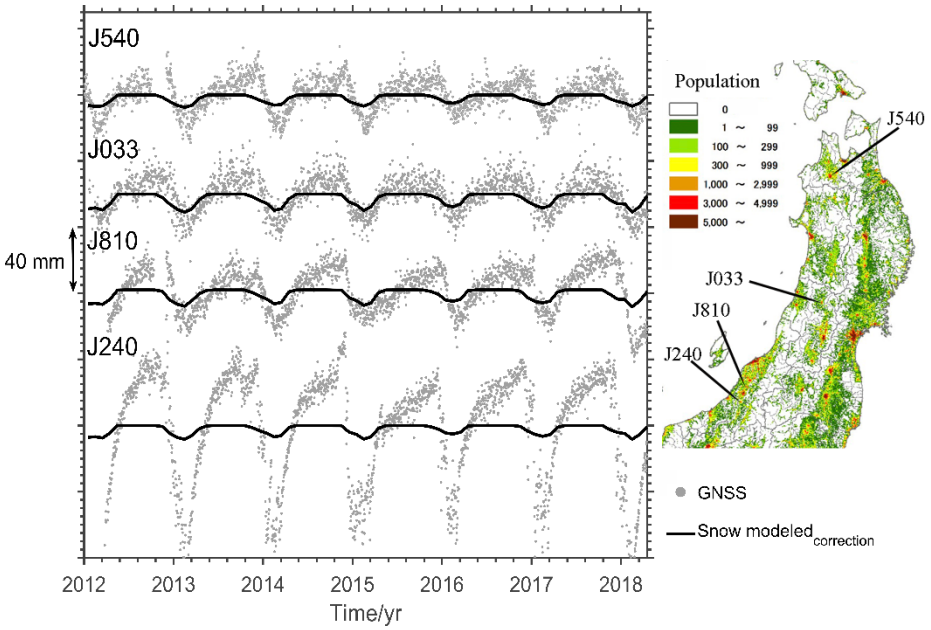


Fig. 10. Up coordinate time series of four urban GNSS stations showing abnormal amplitudes of winter subsidence, much exceeding those calculated by snow loading (black curves). They are located within cities, Hirosaki (J540), Shinjo (J033), Sanjo (J810), and Ojiya (J240). Subsidence of these stations may be largely caused by the water pumping from aquifer to melt snow on roads in city centers. The map to the right shows the population density distribution in northern Honshu in 2015 (www.stat.go.jp/data/mesh/pdf/h27gaiyo.pdf).

Sato et al. (2003) studied a typical example in the Ojiya-city, with population of ~30,000, in the Niigata Prefecture, and showed that vertical crustal movement of the GNSS station is well correlated with the groundwater level. They further confirmed quantitative consistency between the water level and the subsidence. Matsumoto et al. (2018) analyzed the InSAR (Interferometric Synthetic Aperture Radar) data around the city and revealed that the subsidence occurs in two regions with diameter of 1-2 km

and that these regions coincide with the two densely populated areas on both sides of the river penetrating the city. They also showed that the GNSS station J240 (**Fig.10**) is located within one of the subsidence areas detected by InSAR.

There are no such integrated space geodetic and groundwater studies in the other three cities. A recent study by Morishita et al. (2020) systematically mapped 2-dimensional seasonal crustal movements in the Echigo Plain, the coastal plain including the Ojiya-city (J240) and the Sanjo-city (J810). They identified the areas of large winter subsidence around those cities. From these pieces of evidence, the winter subsidences shown in **Fig.10** would include significant contributions from groundwater pumping.

Such groundwater pumping does not take place in Hokkaido, where water sprinkled on road would soon freeze in winter and endanger the traffic. Considering the sparsity of large cities in the studied area and the limited spatial extents of the subsidence area as Matsumoto et al. (2018) and Morishita et al. (2020) revealed using InSAR, GNSS stations influenced by winter groundwater pumping would not be the majority. This is also supported by **Fig. 9B** demonstrating that most GNSS stations show winter subsidences consistent with those calculated from snow loading.

In the Kanto District, farmers pump groundwater for water impoundment to rice fields in late spring. Anomalous vertical movements recorded at Tsukuba correlate well with the local groundwater level (Munekane et al., 2004). However, such groundwater pumping for irrigation is uncommon in the snowy regions in NE Japan, rich in surface water fed by snow in mountains.

Several stations in inland mountainous regions show subsidence much larger than those calculated by snow loading, e.g., J046, G138, J970, J279 in **Fig. S4**. We think this shows a side effect of the altitude correction of snow depths. As explained in Section 3.1, we converted snow depth data to those expected at prefecture-average altitudes. This would have resulted in underestimation of snow loading in regions with altitude higher than the prefectural averages.

5.2.2 Snow accretion to radomes

Heki and Jin (2023) demonstrated another kind of artificial subsidence caused by extra delay of microwave signals due to snow accreted onto radomes using several GNSS stations in Hokkaido. Apparent subsidences of this kind typically occur as short-term (from a few days to a week) events synchronized with large snowfall events under relatively warm air temperatures. They increase gradually and recover suddenly as the snow falls off the radome. Such fake subsidence signals can be discriminated from real ones because they are accompanied by drops of signal-to-noise ratio (SNR) (Heki and Jin, 2023).

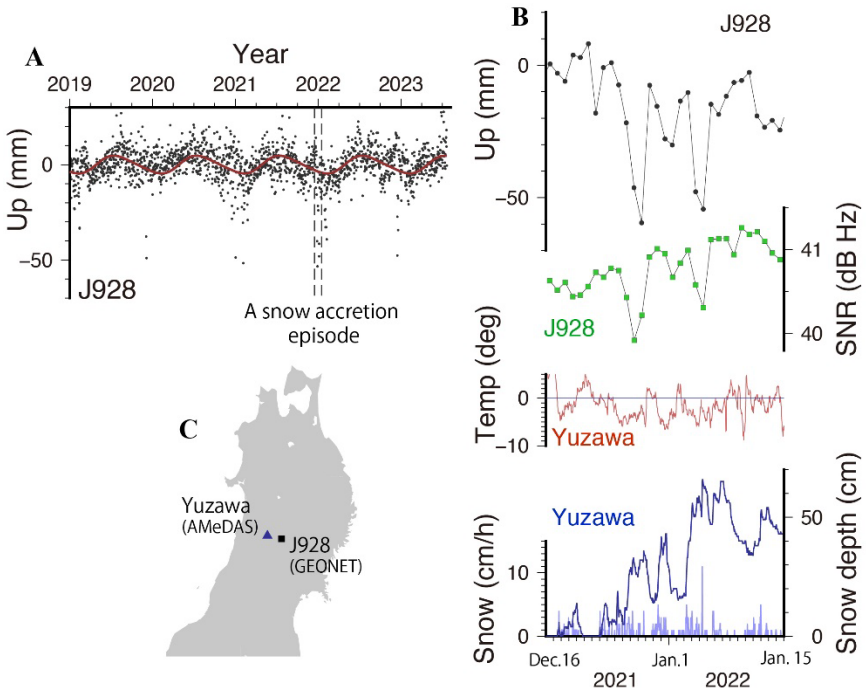


Fig. 11. (A) Time series of vertical position of J928 in NE Honshu (**C**), where short-term large subsidence events are recognized almost every winter. **(B)** One such episode in the period within ±15 days of 2022.0 (between two vertical dashed lines in **A**) is enlarged and plotted together with SNR changes. The hourly temperature, snow depth, and snowfall at the Yuzawa AMeDAS station are also plotted (**C**). Apparent short-term subsidence of ~5 cm occurring twice around 2022.0 is accompanied by simultaneous decrease of SNR possibly caused by snow accretion to the antenna radome.

We also find that apparent subsidence due to snow accretion occurs at several stations in Honshu almost every winter. **Fig. 11A** shows a typical case for the station J928**.** We focus on one such abnormal subsidence episode during the 2021-2022 winter. The

subsidence episode lasted for a few days and is synchronized with the SNR drop nearly proportional to the apparent subsidence (**Fig.11B**). The ratio between the SNR drops and the amount of apparent subsidence is consistent with examples in Hokkaido reported in Heki and Jin (2023).

We performed a simple numerical experiment assuming a similar case to J928, i.e., a snow accretion episode occurs every January and cause 5 cm fake subsidence lasting a week. This will cause an increase of the subsidence in average seasonal change curves of ~3 mm. At J928, the observed winter subsidence is ~6.8 mm while only ~2.8 mm is expected from snow loading (the amplitude factor shown in **Fig.9** is 2.3). In this case, the excessive subsidence is mostly explained by the snow accretion. However, typical fake subsidence signatures as seen in **Fig.11** can be found only at a small number of stations. Because frequent occurrences of snow accretion would require certain conditions, e.g., weak winds around the radome, the snow accretion contribution to abnormal winter subsidence would not be a major factor.

5.3 Origin of the two types of seasonal subsidence

5.3.1 Crustal subsidence due to seasonal changes in ocean load

In Section 4.1, we showed that the winter subsidences of GNSS stations show two types, strong sharp peaks and broad weak peaks (**Fig.5**). The former is often seen in inland stations, and can be understood straightforward by snow loading. Here we discuss the origin of the latter, i.e., factors responsible for the broad winter subsidence peaks. First, we discuss if contribution of the ocean loading by the Japan Sea can explain this using the seasonal ocean loading shown in Section 3.2.

As shown in **Fig.3**, the Japan Sea shows a broad mass peak from late autumn to winter, and its waveforms match with the broad winter subsidence peaks often found in coastal stations (**Fig.5B**). Here we evaluate if the ocean loading is large enough to govern winter subsidence at coastal GNSS stations. We use monthly averages of all the grids in **Fig.3** by GRACE SH and the best-fit seasonal curve as the input. **Fig. 12** indicates seasonal vertical crustal movements at GNSS stations in NE Japan caused by

seasonal ocean loading in the Japan Sea. The peak ocean mass can depress the ground by no more than 1 mm in peak-to-peak even at coastal GNSS stations. As mentioned in Section 3.2.1, the seasonal mass changes in the Pacific Ocean are even less. We definitely need another factor to broaden the winter subsidence peak at these stations.

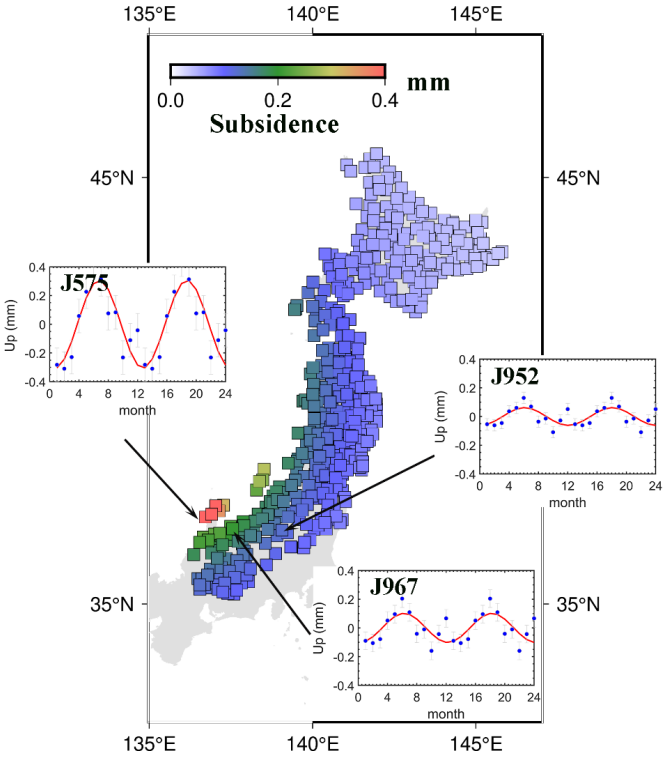


Fig. 12. Vertical crustal movements at GNSS stations expected by the seasonal changes of the ocean loading in the Japan Sea. We calculated monthly displacements of GNSS stations using seasonal ocean loading changes from GRACE SH at all the grid points shown in **Fig. 3**. Their amplitudes are too small to influence seasonal vertical crustal movements in NE Japan.

5.3.2 Additional load in coastal area in spring

Fig.13 compares average observed seasonal change curves and those by the realistic snow loading model at three stations along the Japan Sea coast. At these stations, recovery from maximum subsidence in winter occurs later than snow melting. In contrast, onset of the subsidence in early winter and amounts of the subsidence in February and March are consistent with the snow loading model. In short, we need additional load causing a few mm subsidences for these stations from spring to early summer.

What kind of load causes the extra subsidence at these stations from spring to early summer? **Fig. 6** shows that stations showing broad winter subsidence peaks are mainly distributed in the coastal plains. Japanese communities traditionally have settled in flat areas along rivers to utilize the fresh water for growing rice, the staple food in Japan. In middle spring, farmers impound rice fields with water from rivers. Because such water comes from snow accumulated in mountains during winter, rice fields may delay the decay of snow load by temporarily holding meltwater in lowland plains. Natural lakes and wetlands would also exert similar contributions, but their areas are much smaller than rice fields in the Japanese Islands. We conduct a simple numerical experiment to compute subsidence of GNSS stations due to water loads in the rice fields.

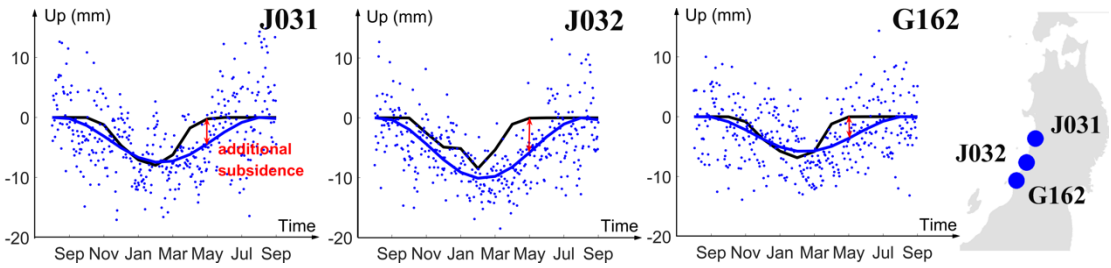


Fig. 13. Observed seasonal vertical movements of three GNSS stations near the Japan Sea coast showing broad winter subsidence peaks (blue curves), and subsidence inferred from the corrected snow loading (black curves, same as those in **Fig.8**). There should be additional mass causing subsidence over a period from spring to early summer. The distribution of this additional subsidence in mid-May is given in **Fig. S5**.

After getting the corrected snow contribution to the observed seasonal vertical movements of coastal stations (here we select stations having the index in **Fig.6** <50%), we estimate the extra subsidence in mid-May relative to summer (**Fig. 13**) and show their distribution in **Fig. S5**. Here we evaluate if reasonable amount of water in rice fields cause such subsidences.

5.3.3 Spring subsidence by water loading in rice fields

We assume these rice fields exist in flat lands with altitude below a certain threshold

and inferred their distribution using the topographic data (NOAA National Centers for Environmental Information, 2022). We then calculate the subsidence of the GNSS stations caused by water loading in rice fields. The whole procedure has five steps, (1) identify area with altitude lower than a threshold and assume them rice fields, (2) get the sums of such areas for individual prefectures, (3) tune the threshold to maximize the consistency of the total area of rice fields with the sum of agricultural area in individual prefectures, (4) assume uniform thickness water loading for 0.167° × 0.167° rectangles distributed over rice fields, and (5) calculate subsidence of GNSS stations using the Green's function and compare with **Fig.S4**. We used the agricultural area data from www.mlit.go.jp/river/toukei_chousa/kasen/jiten/toukei/birn27p.html.

For the step (3), we adopt 100 m for the altitude threshold (blue area in **Fig. 14A**) because of high consistency with agricultural areas from the statistical reports (we exclude Eastern Hokkaido, where summer temperatures are not high enough to grow rice). Then, we optimized the water thickness over rice fields by repeating the steps (4) and (5). In our case, we found 47 cm gives the optimum water thickness. Typical surface water thickness in rice fields is ~10 cm (e.g., Nishida et al., 2017). However, it is empirically known that we need much more water because soil beneath the surface must be saturated with water to hold the surface water. Hence, actually required water thickness in spring rice fields would much exceed 10 cm. In the present case, 37 cm (i.e., 47 cm – 10 cm) water may correspond to soil moisture and groundwater beneath rice fields.

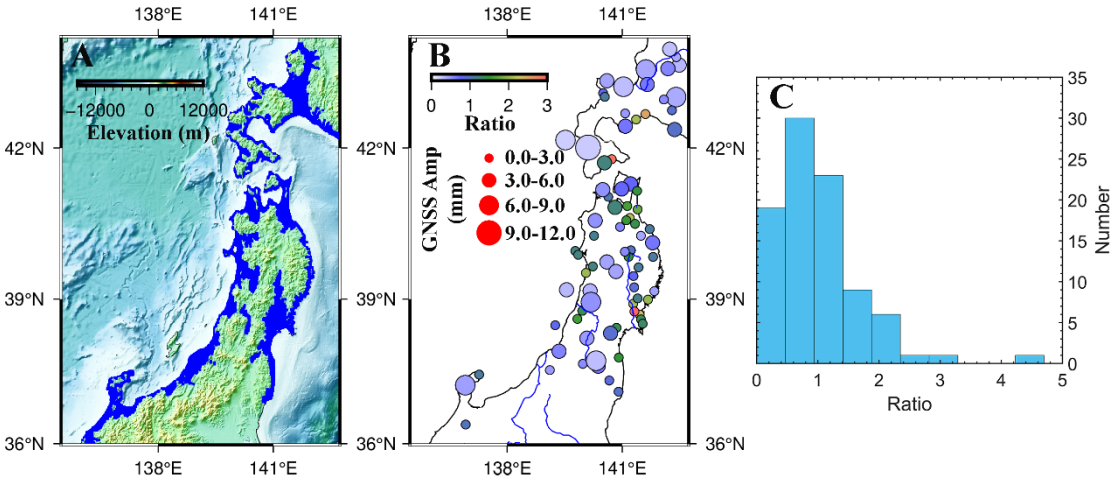


Fig. 14. (**A**) The blue-colored regions represent the area lower than threshold altitude (100 m). (**B**) Map of the ratio of the observed and calculated subsidences by assuming uniform water thickness of 47 cm over the blue regions (rice fields) in **(A)**. (**C**) A histogram of the ratio shown in (B). The water thickness is optimized to bring the average ratio unity.

We here test its sensitivity to the assumption. By increasing the altitude threshold (nominal value is 100 m), rice field area would expand. Then, the water thickness needed to explain the spring subsidence would decrease. Here we repeated the calculation assuming the altitude thresholds of 150 m (although this makes the total rice field areas larger than known values). The results (**Fig. S6**) shows that the water thickness we need decrease to 32 cm. Even by increasing the rice field area beyond the realistic value, we still need substantial amount of water (32 – 10 = 22 cm) in addition to surface water.

One concern is the appropriateness to use the Green's function to calculate surface displacements due to water loading. Thick sedimentary layers lie beneath rice fields. Their rigidity, possibly smaller than average upper crust, may let us overestimate the water in the rice fields. As a whole, we think it likely that the delayed recovery from winter subsidence at GNSS stations close to the coasts may come largely from water impoundment in rice fields in lowlands.

6. Conclusions

In this study, we revisited the seasonal crustal movements in NE Japan originally studied by Heki (2001; 2004) focusing two different surface loads, snowpack on land (including delayed loading in spring by meltwater) and water of the Japan Sea. We summarize the findings into five shown below. The point (1) is the confirmation of the earlier study (Heki, 2004), but the points (2)-(5) are the new findings in the present study.

(1) We confirmed the underestimation of the snow depths by AMeDAS stations found by Heki (2004). This is caused by biased deployment of the AMeDAS stations to

low altitude regions. The altitude correction (Heki, 2004) was demonstrated to make them more realistic.

(2) The waveforms of observed seasonal vertical movements of the GNSS stations have two types, those with sharp winter subsidence peaks and those with broad subsidence peaks. They are distributed along the backbone range and in regions close to coasts, respectively.

(3) The winter subsidence can be well explained by the corrected snow loading. However, additional small subsidence in spring is necessary for lowland stations showing broad winter subsidence peaks. We found they are largely explained by delayed decay of snow loading by impoundment of rice fields in lowlands.

(4) We detected some stations suffer from the winter subsidence due to groundwater pumping for melting snow on roads. This is typically seen in snowy urban areas in Honshu where winter temperatures are moderate. We also found some stations suffer from fake subsidence signals due to snow accretion on antennas.

(5) We evaluated seasonal ocean water mass changes in the Japan Sea using GRACE, satellite altimetry and Argo float data. They consistently show ~5.0 cm peak-to-peak seasonal changes with maximum in October. It causes subsidence of only <1 mm peak-to-peak even for coastal GNSS stations. Ocean mass changes have only limited contribution to seasonal vertical movements in NE Japan.

CRediT authorship contribution statement

Shuo Zheng: Methodology, Writing – original draft, Formal analysis, Visualization, Investigation. Kosuke Heki: Methodology, Conceptualization, Supervision, Writing–review & editing, Investigation. Zizhan Zhang: Writing – review & editing. Haoming Yan: Writing – review & editing.

Declaration of Competing Interest

The authors declare that they have no known competing financial interests or personal relationships that could have appeared to influence the work reported in this paper.

Data availability

Data will be made available on request.

Acknowledgments

We thank three referees for constructive comments. We also thank Shuang Yi (Univ. Chinese Acad. Sci.) and Zhe Song (APM, Univ. Chinese Acad. Sci.) for discussion in the early phase of the study. The GNSS daily coordinates used in this study are available from the Nevada Geodetic Laboratory, University of Nevada, Reno (geodesy.unr.edu). The CSR GRACE products used in the study were downloaded from www2.csr.utexas.edu/grace/. The satellite altimeter sea surface height data are available from the COPERNICUS Marine Environment Monitoring Service (marine.copernicus.eu/). The tide gauge data are available from psmsl.org/data/. The ARGO float data were provided by the Scripps Institution of Oceanography (SIO) at the University of California at San Diego (www.argo.ucsd.edu/Gridded_Fields.html). KH is supported by Chinese Academy of Sciences, President's International Fellowship Initiative (Grant 2022VEA0014) and this study was also jointly supported by the NSFCs (Grant Nos. 42174042, 42174100 and 41874098), the Open Fund of Hubei Luojia Laboratory (220100044).

References

Alothman, A.O., Bos, M., Fernandes, R., Radwan, A.M., Rashwan, M., 2020. Annual sea level variations in the Red Sea observed using GNSS. Geophys. J. Int., 221, 826-834. https://doi. org/10.1093/gji/ggaa032.

Argo., 2000. Argo float data and metadata from Global Data Assembly Centre (Argo GDAC), SEANOE. https://doi. org/10.17882/42182.

Argus, D. F., Fu, Y., Landerer, F. W., 2014, Seasonal variation in total water storage in California inferred from GPS observations of vertical land motion, Geophys. Res. Lett. 41, 1971– 1980. https://doi. org/10.1002/2014GL059570.

Blewitt, G., Hammond, W., Kreemer, C., 2018. Harnessing the GPS Data Explosion for Interdisciplinary Science. https://doi. org/10.1029/2018EO104623.

Borsa, A. A. D. C. Agnew, and D. R. Cayan., 2014. Ongoing drought-induced uplift in the western United States, Science, 345, 1587-1590. https://doi. org/10.1126/science.1260279.

Chen, J. L., Wilson, C. R., Tapley, B. D., Save, H.,Cretaux, J.-F., 2017. Long-term and seasonal Caspian Sea level change from satellite gravity and altimeter measurements. J. Geophys. Res. Solid Earth. 122, 2274– 2290. https://doi.org/10.1002/2016JB013595.

Cheng, M. K., J. C. Ries., B. D. Tapley., 2011, Variations of the Earth's figure axis from satellite laser ranging and GRACE. J. Geophys. Res. Solid Earth. 116, B01409. https://doi.org/10.1029/2010JB000850.

Dong, D., Fang, P., Bock, Y., Cheng, M. K., Miyazaki, S., 2002. Anatomy of apparent seasonal

variations from GPS-derived site position time series. J. Geophys. Res. Solid Earth. 107, 2075. https://doi.org/10.1029/2001JB000573.

Drouin, V., Heki, K., Sigmundsson, F., Hreinsdóttir, S., Ófeigsson, B. G., 2016. Constraints on seasonal load variations and regional rigidity from continuous GPS measurements in Iceland, 1997–2014. Geophys. J. Int. 205, 1843–1858. https://doi.org/10.1093/gji/ggw122.

Farrell, W.E., 1972. Deformation of the Earth by surface loads. Rev. Geophys. 10(3), 761–797. https://doi.org/10.1029/ rg010i003p00761.

Fu, Y., Argus, D. F., Landerer, F. W., 2015. GPS as an independent measurement to estimate terrestrial water storage variations in Washington and Oregon. J. Geophys. Res. Solid Earth. 120(1), 552-566. https://doi.org/10.1002/2014JB011415.

Hammond, W. C., Blewitt, G., Kreemer, C., 2016, GPS Imaging of vertical land motion in California and Nevada: Implications for Sierra Nevada uplift, J. Geophys. Res. Solid Earth. 121, 7681–7703. https://doi.org/10.1002/2016JB013458.

Heki, K., 2001, Seasonal modulation of interseismic strain build-up in Northeastern Japan driven by snow loads, Science, 293, 89-92. 2. https://doi.org/10.1126/science.1061056.

Heki, K., 2003. Snow load and seasonal variation of earthquake occurrence in Japan, Earth Planet. Sci. Lett. 207, 159-164. https://doi.org/10.1016/S0012-821X(02)01148-2.

Heki, K., 2004. Dense GPS array as a new sensor of seasonal changes of surface loads, in State of the Planet: Frontiers and Challenges in Geophysics, edited by R. S. J. Sparks and C.J. Hawkesworth, Geophysical Monograph Ser. 150, 177-196, American Geophys. Union, Washington.

Heki, K., Arief, S., 2022. Crustal response to heavy rains in Southwest Japan 2017-2020. Earth Planet. Sci. Lett. 578. https://doi.org/10.1016/j.epsl.2021.117325.

Heki, K., S. Jin., 2023. Geodetic studies on earth surface loading with GNSS and GRACE, Satellite Navigation 4, 24. https://doi.org/10.1186/s43020-023-00113-6.

He, X., Yu, K., Montillet, J.-P., Xiong, C., Lu, T., Zhou, S., 2020. GNSS-TS-NRS: An Open-Source MATLAB-Based GNSS Time Series Noise Reduction Software. Remote Sens, 12(21), 3532. https://doi.org/10.3390/rs12213532

JMA., 2021. Press release from Japan Meteorological Agency on the Japanese climate in year 2020. www.data.jma.go.jp/obd/stats/data/stat/tenko2020.pdf (in Japanese)

Kierulf, H.P., van Pelt, W.J.J., Petrov, L., Dähnn, M., Kirkvik, A.-S. & Omang, O., 2021b. Seasonal glacier and snow loading in Svalbard recovered from geodetic observations, Geophys. J. Int., 229(1), 408-425. https://doi.org/10.1093/gji/ggab482

Matsumoto, S., Kuwabara, M., Yamashita, T., Honda, M., Hayashi, K., Sakai, K., Munekane, H., 2018. Paper presented at the 2018 Fall Meeting of the Geodetic Society of Japan, Kochi, Japan, October 2018.

Matsuo, K., Heki. K., 2012. Anomalous precipitation signatures of the Arctic Oscillation in the time-variable gravity field by GRACE. Geophys. J. Int. 130, 1495-1506. https://doi.org/10.1111/j.1365-246X.2012.05588.x.

Milliner, C., Materna, K., Bürgmann, R., Fu, Y., Moore, A.W., Bekaert, D., Adhikari, S., Argus, D.F., 2018. Tracking the weight of Hurricane Harvey's storm water using GPS data. Sci. Adv., 4(9), eaau2477. https://doi.org/10.1126/sciadv.aau2477.

Morishita, Y., Lazecky, M., Wright, T. J., Weiss, J. R., Elliott, J. R., Hooper, A., 2020. LiCSBAS: An open-source InSAR time series analysis package integrated with the LiCSAR automated

Sentinel-1 InSAR processor. Remote Sensing 12, 424, https://doi.org/10.3390/rs12030424.

Munekane, H., Tobita, M., Takashima, K., 2004. Groundwater-induced vertical movements observed in Tsukuba, Japan. Geophys. Res. Lett. 31, L12608. https://doi.org/10.1029/2004GL020158.

Nishida, K., Mitsuyasu, M., Yoshida, S., Shiozawa, S., 2017. Relationship between water depth and water and soil temperature in a paddy field during rice ripening period. Transactions of The Japanese Society of Irrigation, Drainage and Rural Engineering, 85(2), I_253-I_263.

NOAA National Centers for Environmental Information. 2022: ETOPO 2022 15 Arc-Second Global Relief Model. NOAA National Centers for Environmental Information. https://doi.org/10.25921/fd45-gt74.

Pujol, M., Francoise, M., 2016. Product user manual for sea level SLA products, Copernicus Monitoring Environment Marine Service (CMEMS) (https://resources.marine.copernicus.eu/). https://doi.org/10.48670/moi-00148.

Roemmich, D., W. B. Owens., 2000. The Argo Project: Global ocean observations for understanding and prediction of climate variability, Oceanography, 13, 4 5–50.

Sato, H. P., Abe, K., Ootaki, O., 2003. GPS-measured land subsidence in Ojiya City, Niigata Prefecture, Japan. Engineering Geology 67, 379-390.

Save, H., Bettadpur, S., Tapley, B.D., 2016. High-resolution CSR GRACE RL05 mascons. J. Geophys. Res. Solid Earth, 121, 7547–7569. https://doi.org/10.1002/2016jb013007.

Save, H., 2019. CSR GRACE RL06 Mascon Solutions. Texas data repository Dataverse V1, https://doi.org/10.18738/T8/UN91VR.

Swenson, S., Wahr, J., 2006. Post-processing removal of correlated errors in GRACE data. Geophys. Res. Lett. 33, L08402. https://doi.org/10.1029/2005GL025285.

Swenson, S., Chambers, D., Wahr, J., 2008. Estimating geocenter variations from a combination of GRACE and ocean model output. J. Geophys. Res. Solid Earth 113(B8). https://doi.org/10.1029/2007JB005338

Ueda, T., Kato, A., Johnson, C. W., Terakawa, T., 2024. Seasonal modulation of crustal seismicity in Northeastern Japan driven by snow load. J. Geophys. Res. Solid Earth 129(3), https://doi.org/10.1029/2023JB028217

Van Dam, T.M., Wahr, J.M., 1987. Displacement of the earth's surface due to atmospheric loading – Effects of gravity and baseline measurements. J. Geophys. Res. Solid Earth 92, 1281-1286. https://doi.org/10.1029/JB0092iB02p01281.

Van Dam, T.M., Wahr, J., Lavallée, D., 2007. A comparison of annual vertical crustal displacements from GPS and Gravity Recovery and Climate Experiment (GRACE) over Europe, J. Geophys. Res. Solid Earth 112, B03404. https://doi.org/10.1029/2006JB004335.

Wahr, J., Molenaar, M., Bryan, F., 1998. Time variability of the Earth's gravity field: Hydrological and oceanic effects and their possible detection using GRACE. J. Geophys. Res. Solid Earth 103, 30205–30229. https://doi.org/10.1029/98JB02844.

Yan, J., Dong, D., Bürgmann, R., Materna, K., Tan, W., Peng, Y., Chen, J., 2019. Separation of sources of seasonal uplift in China using independent component analysis of GNSS time series. J. Geophys. Res. Solid Earth 124, 11951–11971. https://doi.org/10.1029/2019JB018139

Zhan, W., Heki, K., Arief, S., Yoshida, M., 2021. Topographic amplification of crustal subsidence by the rainwater load of the 2019 typhoon Hagibis in Japan. J. Geophys. Res. Solid Earth 126, Article e2021JB021845. https://doi.org/10.1029/2021JB021845.

Zheng, S., Heki, K., Zhang, Z., Tokui, Y., Yan, H., 2023. Interference of ocean and land mass changes in seasonal crustal deformation of coastal stations: A case study in northern Australia. Earth Planet. Sci. Lett. 614. https://doi.org/10.1016/j.epsl.2023.118212.

Supplementary materials

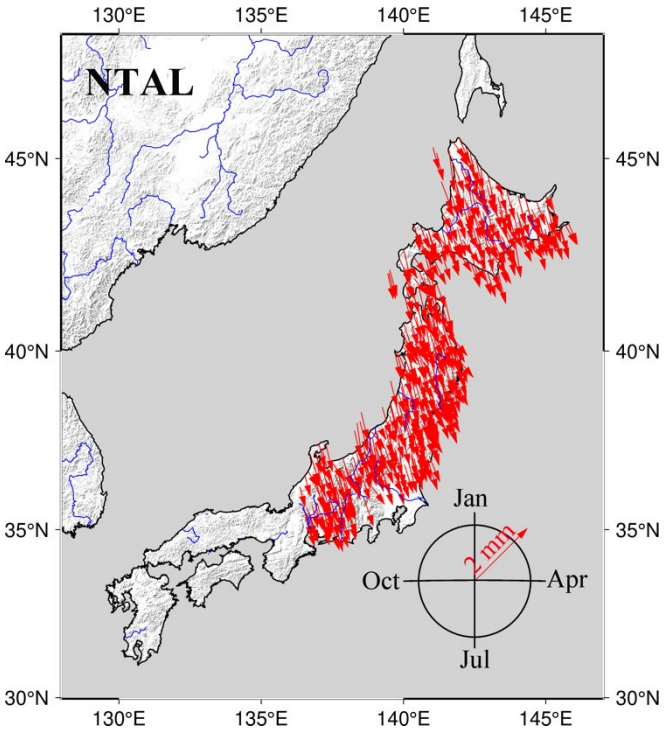


Fig. S1. Annual amplitudes and peak phases of vertical positions due to non-tidal atmospheric loading (NTAL) at GNSS stations in NE Japan. The maximum uplift time is expressed with the azimuth of the arrow measured clockwise from the north (January). The arrow of the legend indicates 2 mm displacement. They are already subtracted before discussing snow loading signals.

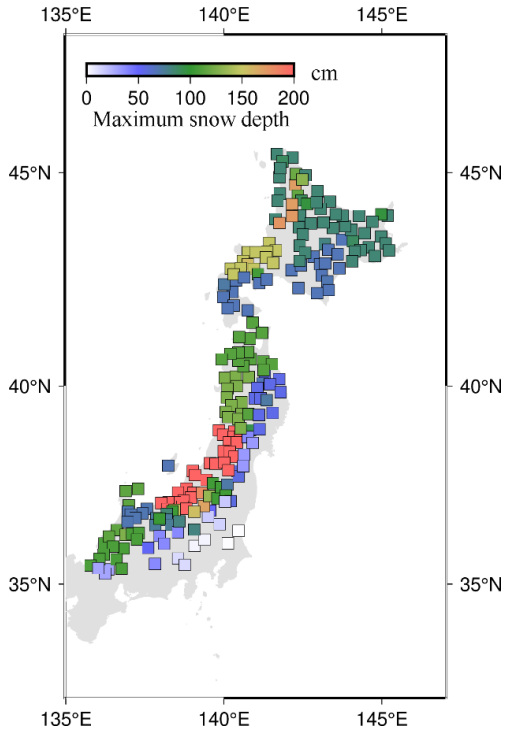


Fig. S2. The altitude-corrected maximum snow depth at AMeDAS sites using the

procedure described in Section 3.1 and in Heki (2004). For each prefecture, we modeled maximum snow depths as a linear function of AMeDAS altitudes. A few of the official prefectures are subdivided into two when enough numbers of snow depth data are available. Using this linear relationship, we converted snow depths to those at prefectural average altitudes.

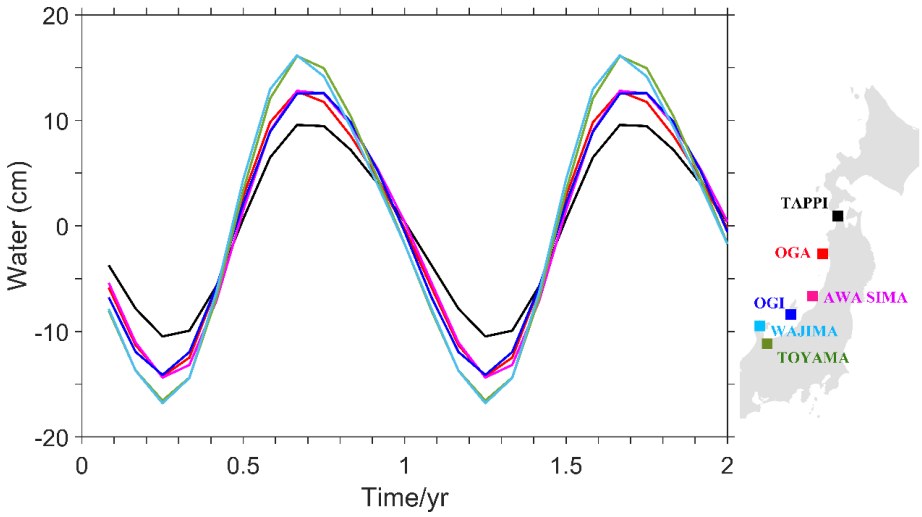


Fig. S3. Average monthly changes of SSH from the tide gauges around the eastern margin of the Japan Sea. Colors of the curves are identical to those used to mark the stations in the map. They show amplitudes of 20-30 cm peak-to-peak, but they largely come from thermal expansion.

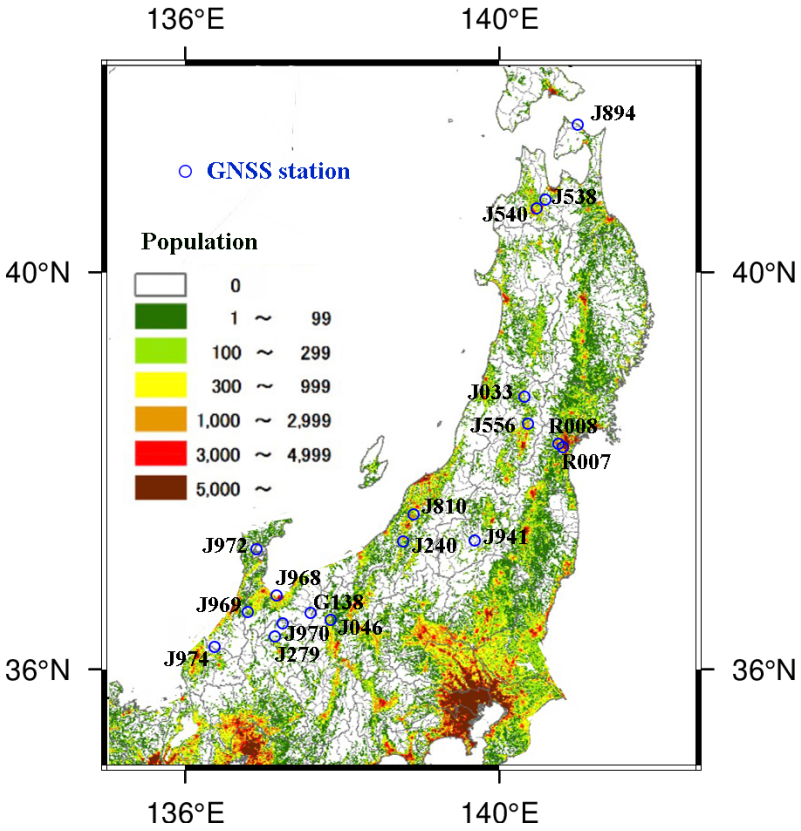


Fig. S4. Population density of NE Japan in 2015 (per mesh of 1 x 1 km) (www.stat.go.jp/data/mesh/pdf/h27gaiyo.pdf) and the GNSS stations showing excessive winter subsidences not explained by snow loading (the amplitude factor shown in **Fig.9** exceeding 3).

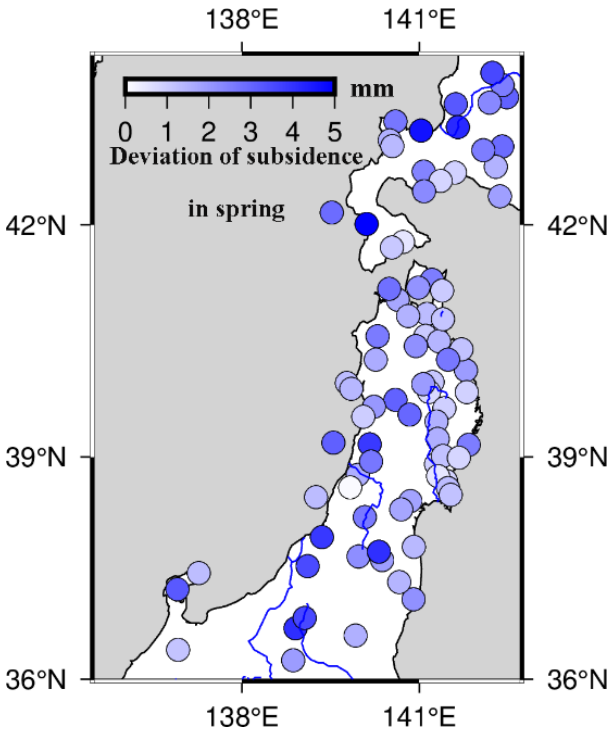


Fig. S5. Additional subsidence in spring for the stations showing broad winter subsidence peaks (here we selected the new index in **Fig.6** lower than 50%) in seasonal vertical movements. They are calculated as the difference at middle May of the observed vertical position from those inferred from snow loads (**Fig.13**).

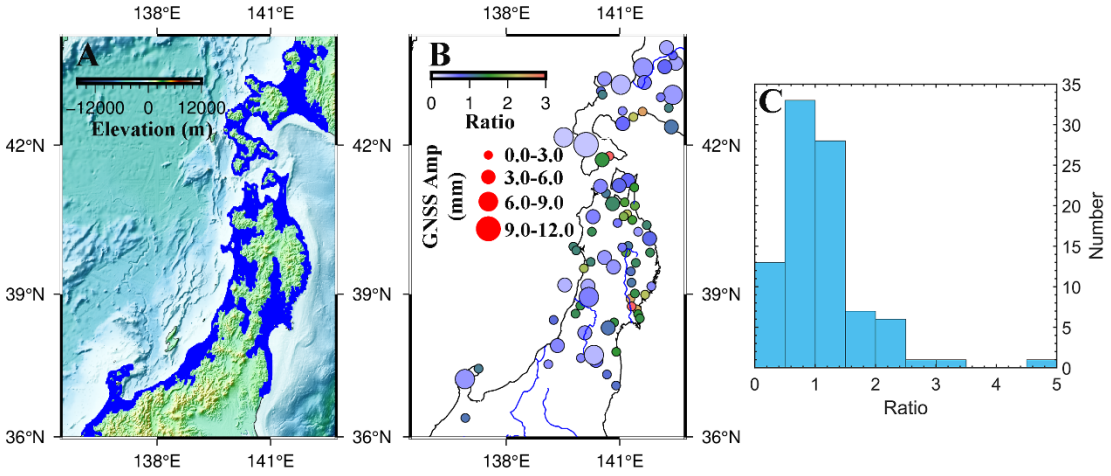


Fig. S6. (**A**) The blue-colored regions repre sent the rice fields assumed as area with the elevation lower than 150 m. (**B**) Map with the colors of the circles showing the ratio of the observed spring subsidence relative to those calculated by water loading in rice fields shown in **A** (32 cm thick). (**C**) The distribution of the ratio. See the caption of **Fig. 14** for detail.